

Observation of a linked loop quantum state

Ilya Belopolski*,^{1,2,†} Guoqing Chang*,³ Tyler A. Cochran*,¹ Zi-Jia Cheng*,¹ Xian P. Yang,¹ Cole Hugelmeyer,⁴ Kaustuv Manna,^{5,6} Jia-Xin Yin,¹ Guangming Cheng,⁷ Daniel Multer,¹ Maksim Litskevich,¹ Nana Shumiya,¹ Songtian S. Zhang,¹ Chandra Shekhar,⁵ Niels B. M. Schröter,⁸ Alla Chikina,⁸ Craig Polley,⁹ Balasubramanian Thiagarajan,⁹ Mats Leandersson,⁹ Johan Adell,⁹ Shin-Ming Huang,¹⁰ Nan Yao,⁷ Vladimir N. Strocov,⁸ Claudia Felser,⁵ and M. Zahid Hasan^{1,7,11,‡}

¹*Laboratory for Topological Quantum Matter and Spectroscopy (B7),*

Department of Physics, Princeton University,

Princeton, New Jersey 08544, USA

²*RIKEN Center for Emergent Matter Science (CEMS), Wako, Saitama 351-0198, Japan*

³*Division of Physics and Applied Physics,*

School of Physical and Mathematical Sciences,

Nanyang Technological University, 21 Nanyang Link, 637371, Singapore

⁴*Department of Mathematics, Princeton University,*

Princeton, New Jersey 08544, USA

⁵*Max Planck Institute for Chemical Physics of Solids,*

Nöthnitzer Straße 40, 01187 Dresden, Germany

⁶*Department of Physics, Indian Institute of Technology Delhi,*

Hauz Khas, New Delhi 110016, India

⁷*Princeton Institute for Science and Technology of Materials,*

Princeton University, Princeton, New Jersey, 08544, USA

⁸*Swiss Light Source, Paul Scherrer Institut, CH-5232 Villigen, Switzerland*

⁹*MAX IV Laboratory, Lund University,*

P.O. Box 118, 221 00 Lund, Sweden

¹⁰*Department of Physics, National Sun Yat-Sen University, Kaohsiung 804, Taiwan*

¹¹*Materials Sciences Division, Lawrence Berkeley*

National Laboratory, Berkeley, CA 94720, USA

(Dated: May 25, 2022)

* These authors contributed equally to this work.

Abstract

Quantum phases can be classified by topological invariants, which take on discrete values capturing global information about the quantum state [1–19]. Over the past decades, these invariants have come to play a central role in describing matter, providing the foundation for understanding superfluids [6, 7], magnets [8, 9], the quantum Hall effect [4, 10], topological insulators [11–15], Weyl semimetals [16–19] and other phenomena. Here we report a remarkable linking number (knot theory) invariant associated with loops of electronic band crossings in a mirror-symmetric ferromagnet [20–26]. Using state-of-the-art spectroscopic methods, we directly observe three intertwined degeneracy loops in the material’s bulk Brillouin zone three-torus, \mathbb{T}^3 . We find that each loop links each other loop twice. Through systematic spectroscopic investigation of this linked loop quantum state, we explicitly draw its link diagram and conclude, in analogy with knot theory, that it exhibits linking number $(2, 2, 2)$, providing a direct determination of the invariant structure from the experimental data. On the surface of our samples, we further predict and observe Seifert boundary states protected by the bulk linked loops, suggestive of a remarkable Seifert bulk-boundary correspondence. Our observation of a quantum loop link motivates the application of knot theory to the exploration of exotic properties of quantum matter.

Quantum topology is powerful in understanding condensed matter systems that exhibit a winding [1–19]. Often, this winding occurs in real space. For example, in a magnetic material, the local magnetization may exhibit a rotating pattern centered around a point in real space, forming a magnetic vortex encoding an integer winding number [3, 8]. Alternatively, the winding may occur in momentum space. For example, in a one-dimensional topological insulator, the quantum-mechanical wavefunctions wind as the momentum scans through the Brillouin zone [4, 5, 10–14]. These two broad paradigms—order parameters, such as magnetization, which wind in real space and quantum wavefunctions which wind in momentum space—capture a vast landscape of topological phases of matter, spanning decades of research by myriad communities of physicists. Real-space order parameter winding further encompasses disclinations in liquid crystals; vortices in superconductors and superfluid ^4He ; and magnetic skyrmions, whose invariants are proposed as the basis for next-generation computing memory and logic [2, 3, 6–9]. On the other hand, momentum-space wavefunction winding is associated with emergent Dirac fermions in two- and three-dimensional topological insulators; Weyl fermions in topological semimetals; and the quantum Hall effect, which sets the prevailing von Klitzing standard of electrical resistance [10–19]. Despite their importance in modern physics, there is no indication that these two paradigms are exhaustive. Novel paradigms for topology promise to deepen our fundamental understanding of nature, as well as enable new quantum technologies.

Recently, there has been considerable interest in node loops, an electronic structure where two bands cross along a closed curve in momentum space [19–21, 27–31]. Away from the crossing curve, the two bands disperse linearly, so that the node loop consists of a cone dispersion persisting along a loop. Within the paradigm of momentum-space wavefunction winding, node loops are topological, with a quantized Berry phase invariant [11–14, 19, 30, 31]. However, in contrast to other electronic structures studied to date [10–19], node loops can link each other, encoding a linking number invariant (Fig. 1a, Extended Data Fig. 1) [22–26]. Unlike the traditional paradigms of winding, this linking number is associated with the composite loop structure of quantum-mechanical band crossings of the Hamiltonian. Such linked node loops offer the possibility of a new bridge between physics and knot theory. It has further been proposed that these links are governed by emergent non-Abelian node loop charges [22] and that the linking number determines the θ angle of the axion Lagrangian in certain node loop phases [25, 32, 33]. Since the three-dimensional condensed matter

Brillouin zone is a three-torus \mathbb{T}^3 , linked node loops also offer the rare possibility of observing links in a space other than ordinary infinite space \mathbb{R}^3 . Moreover, the Seifert surface of the bulk link is associated with topological boundary states, opening the possibility of a unique Seifert bulk-boundary correspondence in quantum matter [34–38].

Ferromagnets with crystalline mirror symmetry naturally give rise to node loops. In this scenario, the ferromagnetic exchange interaction produces spin-split electronic bands which are generically singly-degenerate throughout momentum space, while mirror symmetry protects two-fold band degeneracies along closed curves confined to the momentum-space mirror planes [28]. Such node loops are called Weyl loops, by analogy with the two-fold degeneracy of a Weyl point [16–18, 29–31]. Weyl loops are extremely effective at concentrating Berry curvature, giving rise to giant anomalous Hall and Nernst effects, up to room temperature and promising for technological applications [20, 39–43]. In crystallographic space groups with multiple perpendicular mirror planes, different Weyl loops living in different mirror planes can naturally link each other [21, 26]. The ferromagnet Co_2MnGa exhibits a crystal structure with multiple perpendicular mirror planes and was recently observed to host electronic Weyl loops [20, 21], bringing together the key ingredients for node loop links.

Co_2MnGa crystallizes in the full Heusler structure, with face-centered cubic Bravais lattice; space group $Fm\bar{3}m$ (No. 225); octahedral point group O_h ; and conventional unit cell lattice constant $c = 5.77 \text{ \AA}$ (Fig. 1b, Extended Data Fig. 2). We observe that our Co_2MnGa samples are ferromagnetic, with Curie temperature $T_C = 690 \text{ K}$, consistent with earlier reports [44, 45]. The point group includes mirror planes normal to \hat{x} , \hat{y} and \hat{z} (defined by the conventional unit cell lattice vectors, representative mirror plane shown in orange in Extended Data Fig. 2a), as well as three C_4 rotation symmetries relating any one of these mirror planes to the other two. We first perform a characterization by atomic-level energy-dispersive X-ray spectroscopy (EDS), providing direct structural evidence that our Co_2MnGa samples are crystallographically well-ordered, show the expected lattice constant and exhibit these mirror and rotation symmetries (Fig. 1b). The real-space mirror planes give rise to momentum-space mirror planes, labelled M_1 (normal to \hat{z}); M_2 (\hat{y}); and M_3 (\hat{x} , Fig. 1c). These mirror planes contain the time-reversal invariant momenta X_1 , X_2 and X_3 , sitting at the centers of the square faces of the bulk Brillouin zone.

Motivated by the observation of mirror-symmetry-protected magnetic Weyl loops in Co_2MnGa [20, 21], we explore the electronic structure of our samples on M_1 , M_2 and M_3 .

We perform *ab initio* calculations of Co_2MnGa in the ferromagnetic state, focusing on these three mutually-perpendicular mirror planes. We find that each mirror plane hosts a Weyl loop, and that the three Weyl loops link one another (Fig. 1c, Extended Data Fig. 9). To experimentally investigate this *ab initio* prediction, we carry out angle-resolved photoemission spectroscopy (ARPES) using soft X-ray photons, optimized for exploring bulk electronic states [46, 47]. Without loss of generality, we consider the crystal cleaving plane in our photoemission experiments to be parallel to M_1 . We first acquire a Fermi surface at a fixed incident photon energy $h\nu = 544$ eV, chosen to fix the k_z momentum to this ‘in-plane’ mirror plane (M_1 , Fig. 1d). We observe a diamond-shaped contour centered on X_1 , which traces out a momentum-space trajectory encircling the square top face of the bulk Brillouin zone. We also observe a small circular feature at the corners of the Fermi surface, which arises from an unrelated band at Γ , irrelevant for what follows. We next perform a photon-energy dependence on the same sample, measuring from $h\nu = 500$ to 800 eV, which allows us to access the electronic structure on the ‘out-of-plane’ mirror M_2 (Fig. 1e). We again observe a diamond-shaped loop contour, now centered on X_2 and encircling the square side face of the bulk Brillouin zone. We then rotate the sample by 90° and repeat the same photon-energy dependence to capture the electronic structure on the other ‘out-of-plane’ mirror M_3 . We observe again a similar diamond-shaped loop contour centered on X_3 (Fig. 1f). These systematic observations suggest a family of symmetry-related diamond-shaped loop contours, consistent with the octahedral point group O_h . Each of the three loops is related to the others by rotation symmetry and each lives in one of the three mirror planes.

To further understand the loop electronic structures, we examine energy-momentum photoemission spectra slicing through the M_1 loop (Fig. 2a). We observe two bands which disperse toward each other and meet near the Fermi level, E_F ($E_B = 0$), suggesting a cone dispersion. The presence of a cone dispersion in both slices further shows that the cone persists as we move in momentum space, following the M_1 loop Fermi surface. Since Co_2MnGa is ferromagnetic, we expect generically singly-degenerate bands throughout the Brillouin zone [44, 45]. This suggests a cone dispersion consisting of singly-degenerate branches which exhibit a double degeneracy at the touching points, indicating a Weyl loop electronic structure. To better understand the cone dispersions, we perform *ab initio* calculations of the electronic structure on energy-momentum slices corresponding to these ARPES spectra. The calculation shows a Weyl cone with characteristic two-fold degenerate crossing and linear

dispersion away from the crossing (Fig. 2b). Assembled together, this series of Weyl cones forms a Weyl loop. The ARPES and *ab initio* calculations are in good agreement, further suggesting that we have observed a magnetic Weyl loop on M_1 .

To characterize this Weyl loop using ARPES, we systematically track all cone crossings observed along the full M_1 loop trajectory (Fig. 2c). We then fit the crossings to a two-band effective $k \cdot p$ Hamiltonian for a Weyl loop,

$$H = \sum_{k, a, b \in \{\pm\}} c_{ka}^\dagger h_{ab}(k) c_{kb}, \quad h(k) = f(k)\sigma_z + v_F q_z \sigma_x + g(k)\mathbb{1} \quad (1)$$

Here the c_{ka}^\dagger are fermionic creation operators, k is the crystal momentum, σ_z and σ_x are Pauli matrices, $\mathbb{1}$ is the 2×2 identity and $q_z \equiv k_z - 2\pi/c$ is the \hat{z} component of the momentum measured relative to M_1 , where c is the conventional unit cell lattice constant. This Hamiltonian exhibits a Weyl loop on $q_z = 0$ with trajectory given by $f(k) = 0$, formed from two bands with opposite mirror eigenvalues. From our ARPES spectra, we experimentally extract the full Weyl loop trajectory by fitting to a low-order expansion around X_1 , consistent with the symmetries of the system,

$$f(k) = \gamma(1 + \alpha(k_x^2 + k_y^2) + \beta k_x^2 k_y^2) \quad (2)$$

Here α and β fix the Weyl loop trajectory and the scaling factor γ sets an energy scale. The train of crossing points observed in ARPES is well-captured by $\alpha = -1.23 \pm 0.03 \text{ \AA}^2$ and $\beta = -31.5 \pm 4.1 \text{ \AA}^4$ (Fig. 2c). We also find that our ARPES-extracted Weyl loop trajectory agrees well with the trajectory observed in *ab initio* calculations (Extended Data Fig. 3). The energy dispersion of the Weyl loop is set by $g(k)$, well-described by $g(k) = \delta + \eta \cos(4\theta)$, where $\delta = -75 \pm 17 \text{ meV}$, $\eta = 46 \pm 17 \text{ meV}$, and θ is the ordinary polar angle of k , $\tan \theta \equiv k_y/k_x$. Away from the loop, the bands disperse linearly. To capture this dispersion, we examine a deeper constant-energy photoemission slice intersecting the Weyl loop (Fig. 2d). We observe that the experimental dispersion is well-captured by $\gamma = 0.15 \pm 0.05 \text{ eV}$. The extracted dispersion reaches the Fermi level within experimental resolution, suggesting that the observed Weyl loops are relevant for transport and other low-energy response. This result is consistent with previous reports that Weyl loops play a dominant role in the giant anomalous Hall effect and other exotic transport properties of Co_2MnGa [20, 40–42]. Our analytical model, with all parameters extracted from photoemission spectra, allows us to

achieve a complete experimental characterization of both the momentum trajectory and energy dispersion of the family of Weyl loops (Fig. 2e, Extended Data Fig. 3).

We next investigate the composite structure formed by the three Weyl loops, focusing on the Weyl loop crossing itself (degeneracy curve, shown in cyan in Fig. 2e). The loop crossing disperses in energy, so a constant-energy slice through the electronic structure typically intersects a loop crossing only at several discrete points (for example, the cyan dots in Fig. 2d). However, despite this energy dispersion, we find that the typical ‘radius’ of the Weyl loop, $|k|_{\text{avg}} = 0.66 \text{ \AA}^{-1}$, is much larger than the typical momentum separation of the two branches of the Weyl cone at the Fermi level, $\eta/v_F = 0.07 \text{ \AA}^{-1}$. Since $|k|_{\text{avg}} \gg \eta/v_F$, we can treat the Weyl loop crossing as approximately flat in energy and we can accurately capture its trajectory by examining a constant-energy slice near the Fermi level. Therefore, to understand the composite structure of the Weyl loops, we can focus on the M_1 , M_2 and M_3 Weyl loop Fermi surfaces. We first consider the M_1 and M_2 Weyl loops in an extended zone scheme. We study two adjacent Brillouin zones (Fig. 3a, inset) and zoom in on the momentum-space region around X_1 . By plotting the M_1 and M_2 Weyl loop Fermi surfaces simultaneously in this region of three-dimensional momentum space, we observe that these two loops appear to link each other twice (Fig. 3a). We next consider the M_2 and M_3 Weyl loops and we shift our momentum-space field of view to a region around X_2 . We plot the M_2 and M_3 Weyl loop Fermi surfaces and we again directly observe from our photoemission spectra that the two loops link each other twice (Fig. 3b). Repeating the analogous procedure for X_3 , we observe that the M_3 and M_1 Weyl loops also link twice (Fig. 3c). To estimate the stability of these links, we can measure how far apart one would need to slide two Weyl loops in order to unlink them (Extended Data Figs. 4, 5). From the loop Fermi surfaces, we find that the typical ‘depth’ of the link in momentum-space is $d_{\text{avg}} = 0.58 \pm 0.08 \text{ \AA}^{-1}$, of the same order of magnitude as the radius $|k|_{\text{avg}}$ of the Weyl loop. This large depth suggests that the system lives well within a linked electronic phase. Our three-dimensional momentum-space analysis of the photoemission spectra suggests that each of the M_1 , M_2 and M_3 Weyl loops links each other Weyl loop twice, forming a robust linked structure.

To further explore this link, we examine all three Weyl loops simultaneously using the experimentally-extracted loop trajectory, Eq. 2. In an extended zone scheme, we plot the M_1 , M_2 and M_3 Weyl loops around six nearby X points, so that two redundant copies of

each Weyl loop are included (Fig. 4b). We find that the M_1 Weyl loop links both the M_2 and M_3 Weyl loops; the M_2 Weyl loop links both the M_3 and M_1 loops; and similarly for the M_3 loop. This suggests that the three Weyl loops together form a single composite linked structure. By plotting additional redundant copies of the loops in higher Brillouin zones, we can form a Weyl loop network extending outward to infinity. To more deeply explore this linked structure, we examine energy-momentum photoemission slices tangential to all three loops near their extrema (Fig. 4a). All slices exhibit a cone dispersion, consistent with the Weyl loop electronic structure. Moreover, we find quantitative agreement between the Weyl loop extrema expected from Eq. 2 and the locations of the photoemission cone dispersions, for all three loops. This agreement again suggests the observation of a composite structure of three interwoven Weyl loops. To better visualize the complete link structure, we construct a link diagram for our Weyl loops. In such a link diagram, we flatten the link from three to two dimensions while preserving the link information using an over/under notation (illustrated for the example of a Hopf link, Fig. 4c). Because the Weyl loop link lives in the periodic momentum space of the crystal, we flatten the link into the surface Brillouin zone. Moreover, because our analysis shows that all three Weyl loops are symmetry-related, we choose the (111) surface Brillouin zone (Extended Data Fig. 2), which treats X_1 , X_2 and X_3 equivalently (Fig. 4d). The resulting link diagram shows three loops straddling the edges of the surface Brillouin zone (Fig. 4e). We observe that the link wraps around \mathbb{T}^3 in all three momentum-space directions. This behavior suggests that the link is geometrically essential, in the sense that it cannot be smoothly perturbed to live entirely within a local region of the Brillouin zone. The link diagram further shows that each loop is linked with each other loop exactly twice. This gives 2 for the geometric linking number, defined as the minimal number of crossing changes between link components needed to separate the components. The geometric linking number of the composite Weyl loop structure can then be written as $(2, 2, 2)$, where the first entry in the list corresponds to the linking number between M_1 and M_2 , the second entry between M_2 and M_3 , and the third entry between M_3 and M_1 . By analogy with topological insulators and Weyl point semimetals, this Weyl loop link is expected to be stable under arbitrary, small, symmetry-preserving perturbations of the electronic structure.

Having systematically characterized the link structure in the bulk of Co_2MnGa , we next consider its topological surface states. Unlinked loop nodes host conventional drumhead

surface states, which fill a simply connected region of momentum space in the surface Brillouin zone. By contrast, linked loops exhibit an alternating pattern of topologically distinct regions where surface states are either present or suppressed, and which are pinned together at generic points in momentum space. This topological structure is captured by the Seifert surface, defined as a three-dimensional surface which has the link as its boundary [34]. For a condensed matter system, we consider a Seifert surface defined in (k_x, k_y, k_z) and bounded by the linked loop nodes, with energy axis collapsed. For the minimal case of a Hopf link, the Seifert surface exhibits a branched structure which ‘wraps’ around the link (Fig. 5a, left). A two-dimensional projection of the Seifert surface then produces alternating filled and empty regions, which meet at characteristic touching points (Fig. 5a, right). In the case of the Weyl loop link which we observe in Co_2MnGa , the Seifert projection on the (111) hexagonal surface Brillouin zone then predicts several alternating regions with and without topological boundary states (blue and white regions, Fig. 5c), exhibiting touching points along $\bar{\Gamma} - \bar{K}$. Since the Seifert surface encodes the linking number [34], the topological boundary states are associated with a Seifert bulk-boundary correspondence. In this correspondence, the linking number of the Weyl loops in the bulk is encoded in a Seifert surface, whose projection gives the topological boundary states. A measurement of the bulk link determines the Seifert boundary states, while a measurement of the Seifert boundary states allows a reconstruction of the bulk linking number. To explore these possible surface states, we examine the (111) surface of our Co_2MnGa samples in *ab initio* calculation and surface-sensitive vacuum ultraviolet (VUV) ARPES. On an energy-momentum cut through the touching point we observe in calculation a pair of surface modes pinned together at the Weyl loops (Figs. 5d). Moreover, our photoemission spectra are consistent with our *ab initio* prediction, suggesting the observation of Seifert boundary states approaching the Weyl loop linking point (Fig. 5e). On iso-energy contours of the electronic structure, we expect to observe arc-like slices of the Seifert states, stretching across the filled regions and connecting the linked Weyl loops. Examining the Fermi surface obtained in calculation, we observe a sharp arc of surface states connecting the linked Weyl loops, consistent with the Seifert projection (Fig. 5f, left). At the same time, the suppressed region exhibits no topological surface states in calculation. Our Fermi surface obtained by VUV-ARPES matches the *ab initio* prediction well (Fig. 5f, right). We observe distinct arcs of states connecting the linked Weyl loops across the topological region, corresponding to the topological sur-

face states observed on the energy-momentum cuts (Figs. 5d, e) and suggestive of Seifert states at the Fermi level in Co_2MnGa . Our *ab initio* calculations and photoemission spectra suggest the observation of Seifert boundary states.

Our photoemission spectra, *ab initio* calculations and theoretical analysis suggest the observation of a loop node link in a quantum magnet. On the sample surface, we further observe Seifert boundary states protected by the bulk link, indicating a Seifert bulk-boundary correspondence. These results establish a new bridge between physics and knot theory, motivating further exploration of links and knots in electronic structures. Moreover, the linked loop state in Co_2MnGa , as well as in other materials, may give rise to exotic response quantized to the linking number, such as a link-quantized topological magneto-electric effect [25, 32, 33, 48]. Since high-symmetry magnetic and correlated materials are abundant in nature, these ideas open the way to understanding the exotic behavior of a wide class of quantum magnets and superconductors, as well as their photonic analogs.

† Electronic address: ilya.belopolski@riken.jp

‡ Electronic address: mzhasan@princeton.edu

- [1] M. Buchanan, The unifying role of topology. *Nat. Phys.* **16**, 818 (2020).
- [2] M. Nakahara, *Geometry, Topology and Physics* (Institute of Physics, 2003).
- [3] P. M. Chaikin, T. C. Lubensky, Topological defects, Chap. 9, *Principles of condensed matter physics* (Cambridge University Press, 1995).
- [4] F. D. M. Haldane, Nobel lecture: Topological quantum matter. *Rev. Mod. Phys.* **89**, 040502 (2017).
- [5] X.-G. Wen, Colloquium: Zoo of quantum-topological phases of matter. *Rev. Mod. Phys.* **89**, 041004 (2017).
- [6] G. E. Volovik, *The Universe in a Helium Droplet* (Oxford University Press, 2003).
- [7] M. M. Salomaa, G. E. Volovik, Quantized vortices in superfluid ^3He . *Rev. Mod. Phys.* **59**, 533 (1987).
- [8] J. Zang, V. Cros, A. Hoffmann, *Topology in Magnetism* (Springer, 2018).
- [9] N. Nagaosa, Y. Tokura, Topological properties and dynamics of magnetic skyrmions. *Nat. Nano.* **8**, 899 (2013).

- [10] J. E. Avron, D. Osadchy, R. Seiler, A topological look at the quantum Hall effect. *Phys. Today* **56**, 38 (2003).
- [11] M. Z. Hasan, C. L. Kane, Colloquium: Topological insulators. *Rev. Mod. Phys.* **82**, 3045 (2010).
- [12] A. Bernevig, *Topological Insulators and Topological Superconductors* (Princeton University Press, 2013).
- [13] C. L. Kane, Topological band theory and the \mathbb{Z}_2 invariant, Chap. 1, *Topological Insulators, Contemporary Concepts of Condensed Matter Science* (Elsevier, 2013).
- [14] A. Bansil, H. Lin, T. Das, Colloquium: Topological band theory. *Rev. Mod. Phys.* **88**, 021004 (2016).
- [15] Y. Tokura, K. Yasuda, A. Tsukazaki, Magnetic topological insulators. *Nat. Rev. Phys.* **1**, 126 (2019).
- [16] M. Z. Hasan, S.-Y. Xu, I. Belopolski, S.-M. Huang, Discovery of Weyl fermion semimetals and topological Fermi arc states. *Ann. Rev. Cond. Matt. Phys.* **8**, 289 (2017).
- [17] M. Z. Hasan, S.-Y. Xu, G. Bian, Topological insulators, topological superconductors and Weyl fermion semimetals: discoveries, perspectives and outlooks. *Phys. Scr.* **2015**, T164 (2015).
- [18] N. P. Armitage, E. J. Mele, A. Vishwanath, Weyl and Dirac semimetals in three-dimensional solids. *Rev. Mod. Phys.* **90**, 015001 (2018).
- [19] C.-K. Chiu, J. C. Y. Teo, A. P. Schnyder, S. Ryu, Classification of topological quantum matter with symmetries. *Rev. Mod. Phys.* **88**, 035005 (2016).
- [20] I. Belopolski, *et al.*, Discovery of topological Weyl fermion lines and drumhead surface states in a room temperature magnet. *Science* **365**, 1278 (2019).
- [21] G. Chang, *et al.*, Topological Hopf and chain link semimetal states and their application to Co_2MnGa . *Phys. Rev. Lett.* **119**, 156401 (2017).
- [22] Q. Wu, A. A. Soluyanov, T. Bzdušek, Non-Abelian band topology in noninteracting metals. *Science* **365**, 1273 (2019).
- [23] Z. Yan, *et al.*, Nodal-link semimetals. *Phys. Rev. B* **96**, 041103(R) (2017).
- [24] M. Ezawa, Topological semimetals carrying arbitrary Hopf numbers: Fermi surface topologies of a Hopf link, Solomon's knot, trefoil knot, and other linked nodal varieties. *Phys. Rev. B* **96**, 041202 (2017).
- [25] P.-Y. Chang, C.-H. Yee, Weyl-link semimetals. *Phys. Rev. B* **96**, 081114 (2017).

- [26] C. Zhong, *et al.*, Three-dimensional Pentagon Carbon with a genesis of emergent fermions. *Nat. Commun.* **8**, 15641 (2017).
- [27] G. Bian, *et al.*, Topological nodal-line fermions in spin-orbit metal PbTaSe₂. *Nat. Commun.* **7**, 10556 (2016).
- [28] H. Watanabe, H. C. Po, A. Vishwanath, Structure and topology of band structures in the 1651 magnetic space groups. *Sci. Adv.* **4**, eaat8685 (2018).
- [29] Y. Wang, R. Nandkishore, Topological surface superconductivity in doped Weyl loop materials. *Phys. Rev. B* **95**, 060506 (2017).
- [30] O. Stenull, C. L. Kane, T. C. Lubensky, Topological phonons and Weyl lines in three dimensions. *Phys. Rev. Lett.* **117**, 068001 (2016).
- [31] R. Nandkishore, Weyl and Dirac loop superconductors. *Phys. Rev. B* **93**, 020506(R) (2016).
- [32] X.-Q. Sun, B. Lian, S.-C. Zhang, Double Helix Nodal Line Superconductor. *Phys. Rev. Lett.* **119**, 147001 (2017).
- [33] B. Lian, C. Vafa, F. Vafa, S.-C. Zhang, Chern-Simons theory and Wilson loops in the Brillouin zone. *Phys. Rev. B* **95**, 094512 (2017).
- [34] H. Seifert, Über das geschlecht von knoten. *Mathematische Annalen* **110**, 571 (1935).
- [35] E. J. Bergholtz, J. C. Budich, F. K. Kunt, Exceptional topology of non-Hermitian systems. *Rev. Mod. Phys.* **93**, 015005 (2021).
- [36] L. Li, C. H. Lee, J. Gong, Emergence and full 3D-imaging of nodal boundary Seifert surfaces in 4D topological matter. *Commun. Phys.* **2**, 135 (2019).
- [37] J. Carlström, M. Stålhammar, J. C. Budich, E. J. Bergholtz, Knotted non-Hermitian metals. *Phys. Rev. B* **99**, 161115 (2019).
- [38] X. Zhang, *et al.*, Tidal surface states as fingerprints of non-Hermitian nodal knot metals. *Commun. Phys.* **4**, 47 (2021).
- [39] A. Sakai, *et al.*, Iron-based binary ferromagnets for transverse thermoelectric conversion. *Nature* **581**, 53 (2020).
- [40] A. Sakai, *et al.*, Giant anomalous Nernst effect and quantum-critical scaling in a ferromagnetic semimetal. *Nat. Phys.* **14**, 1119 (2018).
- [41] S. N. Guin, *et al.*, Anomalous Nernst effect beyond the magnetization scaling relation in the ferromagnetic Heusler compound Co₂MnGa. *NPG Asia Mat.* **11**, 16 (2019).
- [42] G.-H. Park, *et al.*, Thickness dependence of the anomalous Nernst effect and the Mott relation

- of Weyl semimetal Co_2MnGa thin films. *Phys. Rev. B* **101**, 060406 (2020).
- [43] A. Markou, *et al.*, Hard magnet topological semimetals in $x\text{Pt}_3$ compounds with the harmony of Berry curvature. *Commun. Phys.* **4**, 104 (2021).
- [44] P. J. Webster, Magnetic and chemical order in Heusler alloys containing cobalt and manganese. *J. Phys. Chem. Solids* **32**, 1221 (1971).
- [45] H. Ido, S. Yasuda, Magnetic properties of Co-Heusler and related mixed alloys. *J. de Physique* **49**, C8 (1988).
- [46] V. N. Strocov, *et al.*, High-resolution soft X-ray beamline ADDRESS at the Swiss Light Source for resonant inelastic X-ray scattering and angle-resolved photoelectron spectroscopies. *J. Synch. Rad.* **17**, 631 (2010).
- [47] V. N. Strocov, *et al.*, Soft-X-ray ARPES facility at the ADDRESS beamline of the SLS: concepts, technical realisation and scientific applications. *J. Synch. Rad.* **21**, 32 (2014).
- [48] L. Wu, *et al.*, Quantized Faraday and Kerr rotation and axion electrodynamics of a 3D topological insulator. *Science* **354**, 1124 (2016).
- [49] V. N. Strocov, *et al.*, Three-Dimensional Electron Realm in VSe_2 by Soft-X-Ray Photoelectron Spectroscopy: Origin of Charge-Density Waves. *Phys. Rev. Lett.* **109**, 086401 (2012).
- [50] G. Kresse, J. Furthmüller, Efficient iterative schemes for *ab initio* total-energy calculations using a plane-wave basis set. *Phys. Rev. B* **54**, 11169 (1996).
- [51] G. Kresse, D. Joubert, From ultrasoft pseudopotentials to the projector augmented-wave method. *Phys. Rev. B* **59**, 1758 (1999).
- [52] J. P. Perdew, K. Burke, M. Ernzerhof, Generalized gradient approximation made simple. *Phys. Rev. Lett.* **77**, 3865 (1996).

ACKNOWLEDGMENTS

I.B. thanks Nikita Lvov and Zoltán Szabó for discussions on linking numbers. The authors thank D. Lu and M. Hashimoto at Beamline 5-2 of the Stanford Synchrotron Radiation Lightsource (SSRL) at the SLAC National Accelerator Laboratory, CA, USA for support. I.B. and D.M. thank Takayuki Muro for experimental support during preliminary ARPES measurements carried out at BL25SU of SPring-8 in Hyogo, Japan. I.B. thanks Biao Lian for discussions on the topological magneto-electric effect. I.B., T.A.C., X.P.Y. and D.M.

thank Jessica McChesney and Fanny Rodolakis for experimental support during preliminary ARPES measurements carried out at BL29 of the Advanced Photon Source (APS) in Illinois, USA. I.B. acknowledges discussions with Boris Belopolski on Savitzky-Golay analysis. G.C. acknowledges the support of the National Research Foundation, Singapore under its NRF Fellowship Award (NRF-NRFF13-2021-0010) and the Nanyang Assistant Professorship grant from Nanyang Technological University. T.A.C. acknowledges support by the National Science Foundation Graduate Research Fellowship Program under Grant No. DGE-1656466. A.C. acknowledges funding from the Swiss National Science Foundation under Grant No. 200021-165529. The authors acknowledge synchrotron radiation beamtime at the ADDRESS beamline of the Swiss Light Source of the Paul Scherrer Institut in Villigen, Switzerland under Proposals 20170898, 20190740 and 20191674. The authors further acknowledge use of Princeton’s Imaging and Analysis Center (IAC), which is partially supported by the Princeton Center for Complex Materials (PCCM), a National Science Foundation (NSF) Materials Research Science and Engineering Center (MRSEC; DMR-2011750). This research used resources of the Advanced Photon Source, a U.S. Department of Energy (DOE) Office of Science User Facility operated for the DOE Office of Science by Argonne National Laboratory under Contract No. DE-AC02-06CH11357. The authors acknowledge beamtime at BL25SU of SPring-8 under Proposal 2017A1669 and at BL29 of the APS under Proposals 54992 and 60811. K.M. and C.F. acknowledge financial support from the European Research Council (ERC) Advanced Grant No. 742068 “TOP-MAT”. C.F. acknowledges the DFG through SFB 1143 (project ID. 247310070) and the Würzburg-Dresden Cluster of Excellence on Complexity and Topology in Quantum Matter ct.qmat (EXC2147, project ID. 39085490). M.Z.H. acknowledges visiting scientist support at Berkeley Lab (LBNL) during the early phases of this work. Work at Princeton University was supported by the Gordon and Betty Moore Foundation (Grants No. GBMF4547 and No. GBMF9461; M. Z. H.). The ARPES and theoretical work were supported by the United States Department of Energy (US DOE) under the Basic Energy Sciences programme (Grant No. DOE/BES DE-FG-02-05ER46200; M. Z. H.). Use of the Stanford Synchrotron Radiation Lightsource (SSRL), SLAC National Accelerator Laboratory, is supported by the U.S. Department of Energy, Office of Science, Office of Basic Energy Sciences, under Contract No. DE-AC02-76SF00515. The authors acknowledge MAX IV Laboratory for time on the BLOCH Beamline under Proposal 20210268. Research conducted at MAX IV, a Swedish na-

tional user facility, is supported by the Swedish Research council under contract 2018-07152, the Swedish Governmental Agency for Innovation Systems under contract 2018-04969, and Formas under contract 2019-02496.

AUTHOR CONTRIBUTIONS

I.B., G. Chang, T.A.C. and M.Z.H. initiated the project. I.B., T.A.C., Z.-J. C. and M.Z.H. acquired and analyzed ARPES spectra with help from X.P.Y., D.M., J.-X.Y., M.L., N.S. and S.S.Z. ARPES measurements were supported by N.B.M.S., A.C., C.P., B.T., M.L., J.A. and V.N.S. G. Chang performed the first-principles calculations. I.B. performed the $k \cdot p$ model analysis with help from G. Chang and S.-M.H. I.B. performed the linking number analysis with help from C.H. G. Cheng and N.Y. performed the scanning transmission electron microscopy measurements. K.M., C.S. and C.F. synthesized and characterized the single crystals. I.B. wrote the manuscript with contributions from all authors.

COMPETING INTERESTS

The authors declare no competing interests.

METHODS

Single crystal growth: Co₂MnGa single crystals were grown using the Bridgman-Stockbarger method. A polycrystalline ingot was first prepared using an induction melt technique, with a stoichiometric mixture of Co, Mn and Ga metal pieces of 99.99% purity. Then the powdered material was poured into an alumina crucible and sealed in a tantalum tube. Growth temperatures were controlled using a thermocouple attached to the bottom of the crucible. During the heating cycle, the material was melted at temperatures above 1200°C and then slowly cooled below 900°C.

Angle-resolved photoemission spectroscopy: Soft X-ray ARPES measurements were carried out at the ADDRESS beamline of the Swiss Light Source in Villigen, Switzerland under vacuum better than 5×10^{-11} Torr and a temperature of 16 K [46, 47, 49]. Rod-shaped

single crystals of Co_2MnGa oriented along the conventional unit cell \hat{z} direction were cleaved *in situ* at base temperature. The constant-energy cuts were symmetrized about M_x and M_{xy} (Fig. 1d), M_x and M_{xz} (Fig. 1e) and M_y and M_{yz} (Fig. 1f). The high-symmetry energy-momentum cuts were similarly symmetrized about M_x , M_y or M_z , as appropriate and consistent with the nominal symmetries of the crystal (Fig. 4a). A background was removed from the photoemission spectra by a fixed intensity cutoff (raw, unsymmetrized data in Extended Data Figs. 6, 7, 8). For the Fermi surfaces acquired at $h\nu = 544$ eV, the nominal energy resolution was $\delta E = 75$ meV; for the photon-energy dependences, the nominal energy resolution varied from $\delta E = 75$ meV at $h\nu = 500$ eV to $\delta E = 125$ meV at $h\nu = 800$ eV. The angular resolution was better than 0.2° in all cases. The Fermi surfaces were binned in an energy window of ± 38 meV (Fig. 1d) and ± 25 meV (Fig. 1e,f) around E_F . Vacuum ultraviolet ARPES measurements were carried out at Beamline 5-2 of the Stanford Synchrotron Radiation Lightsource in Menlo Park, CA, USA at $\delta E = 15$ meV and temperature 20 K.

Ab initio calculations: The electronic structure of Co_2MnGa in the ferromagnetic phase was calculated within the density functional theory (DFT) framework using the projector augmented wave method as implemented in the VASP package [50, 51]. The generalized gradient approximation (GGA) [52] and a Γ -centered k -point $12 \times 12 \times 12$ mesh were used. Ga s, p orbitals and Mn, Co d orbitals were used to generate a real space tight-binding model, from which Wannier functions were determined. The Fermi level in DFT was shifted to match the ARPES.

Scanning transmission electron microscopy: Thin lamellae for microstructure characterization were prepared from bulk single crystals by focused ion beam cutting using a ThermoFisher Helios NanoLab G3 UC DualBeam system (FIB/SEM). Atomic resolution high-angle annular dark-field (HAADF) scanning transmission electron microscopy (STEM) imaging and atomic-level energy-dispersive X-ray spectroscopy (EDS) mapping were performed on a double Cs-corrected ThermoFisher Titan Cubed Themis 300 scanning/transmission electron microscope (S/TEM) equipped with an X-FEG source operated at 300 kV with a Super-X EDS system.

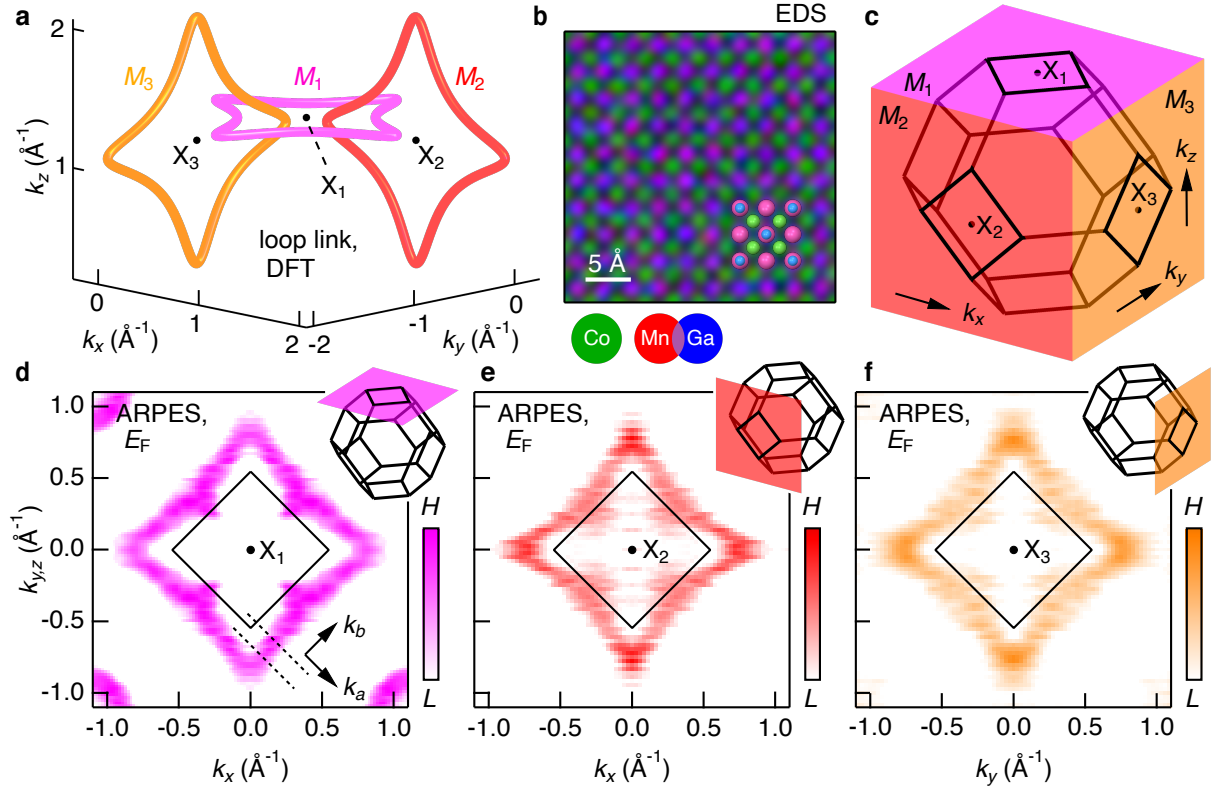


FIG. 1: **Signatures of linked node loops in Co₂MnGa.** **a**, Weyl loops in the electronic structure of Co₂MnGa, predicted by density functional theory (DFT). Three distinct Weyl loops are confined to the three mirror planes M_1 , M_2 and M_3 , in such a way that the loops link one another (additional copies of the loops in higher Brillouin zones not shown). **b**, Element-resolved crystal structure of Co₂MnGa along the [001] direction, acquired by atomic-level energy-dispersive X-ray spectroscopy (EDS). Atomic columns consist either entirely of cobalt (green) or alternating manganese (red) and gallium (blue). **c**, Bulk Brillouin zone (black truncated octahedron) of Co₂MnGa with three mirror planes indicated, M_1 (magenta, constant k_z), M_2 (red, constant k_y) and M_3 (gold, constant k_x). Each mirror plane contains square faces of the Brillouin zone. The high-symmetry momentum-space points at the center of each square are marked X_1 , X_2 , X_3 . **d**, Fermi surface acquired by angle-resolved photoemission spectroscopy (ARPES) at incident photon energy 544 eV, corresponding to M_1 . **e**, Out-of-plane Fermi surface acquired on the same Co₂MnGa sample by an ARPES photon energy dependence from 500 eV to 800 eV in steps of 2 eV, corresponding to M_2 . **f**, Analogous out-of-plane Fermi surface corresponding to M_3 , again on the same sample.

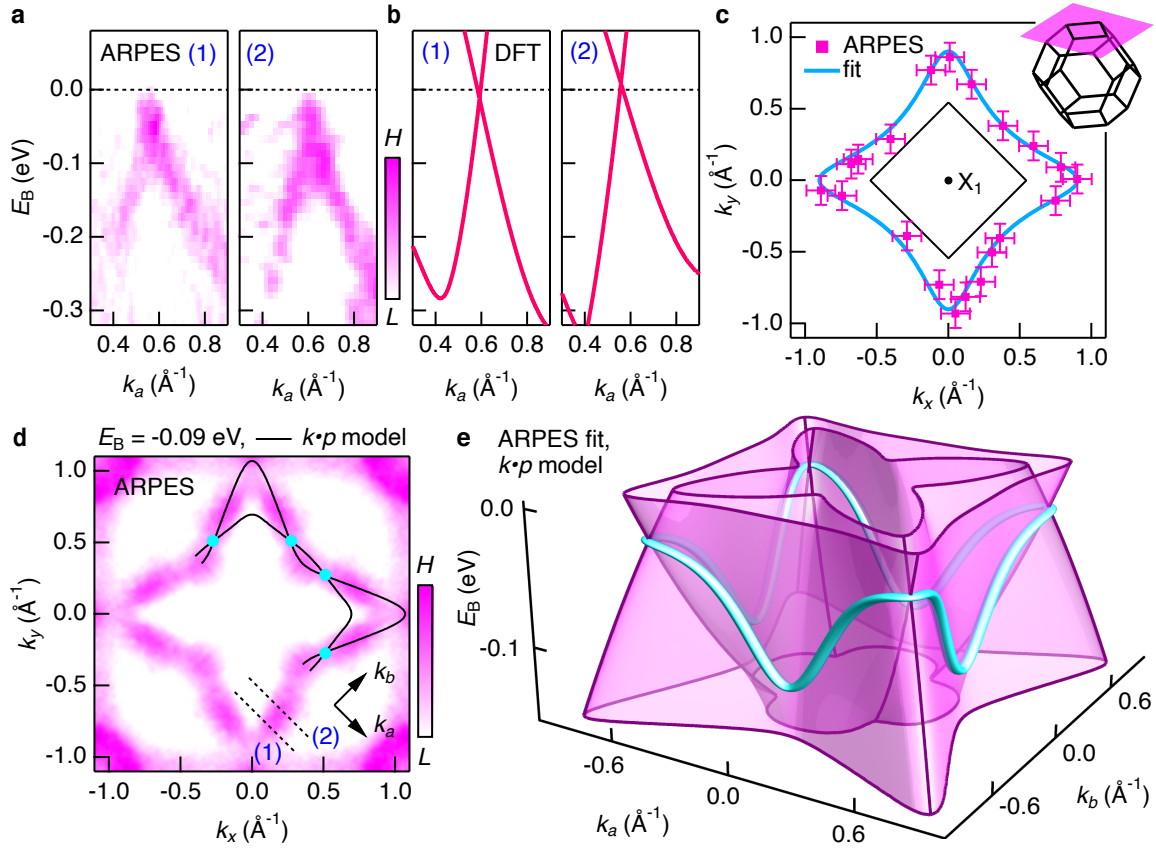


FIG. 2: **Weyl loop trajectory in Co_2MnGa .** **a**, Energy-momentum photoemission slices through the loop Fermi surface (slice locations marked by the dotted lines in (d) and Fig. 1d). **b**, Energy-momentum slices through the Weyl loop from DFT, showing a Weyl loop cone (slice locations marked in Extended Data Fig. 3c). **c**, Cone locations (magenta squares) systematically extracted from cone dispersions observed in photoemission spectra on M_1 . Experimental loop trajectory extracted by fitting to the cone locations (cyan, see main text). The binding energy axis is collapsed. **d**, Constant-energy photoemission slice with analytical model of the Weyl loop (black lines). This slice intersects the Weyl loop at a discrete set of points (cyan dots). **e**, Dispersion of an effective $k \cdot p$ Hamiltonian for the Weyl loop, capturing the experimental loop trajectory.

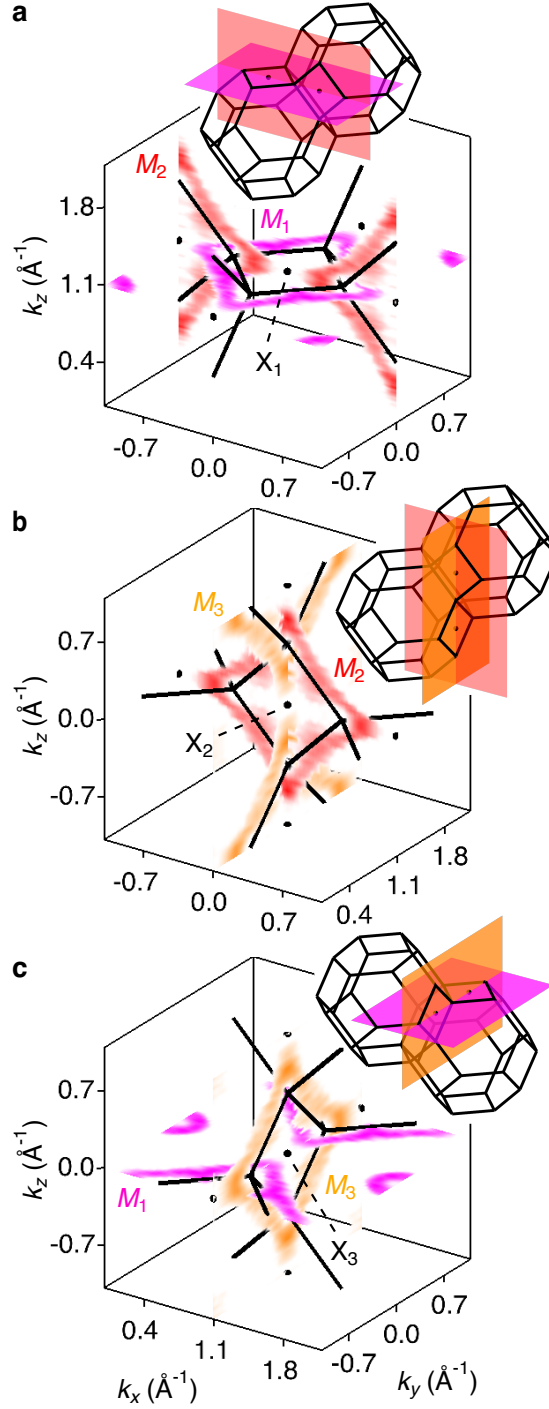


FIG. 3: **Linked Weyl loops in Co_2MnGa .** **a**, M_1 and M_2 loop Fermi surfaces from adjacent bulk Brillouin zones, plotted in an extended zone scheme, exhibiting a link structure. Inset: M_1 and M_2 plotted across multiple Brillouin zones. **b**, M_2 and M_3 loop Fermi surfaces from adjacent bulk Brillouin zones. **c**, M_3 and M_1 loop Fermi surfaces from adjacent bulk Brillouin zones.

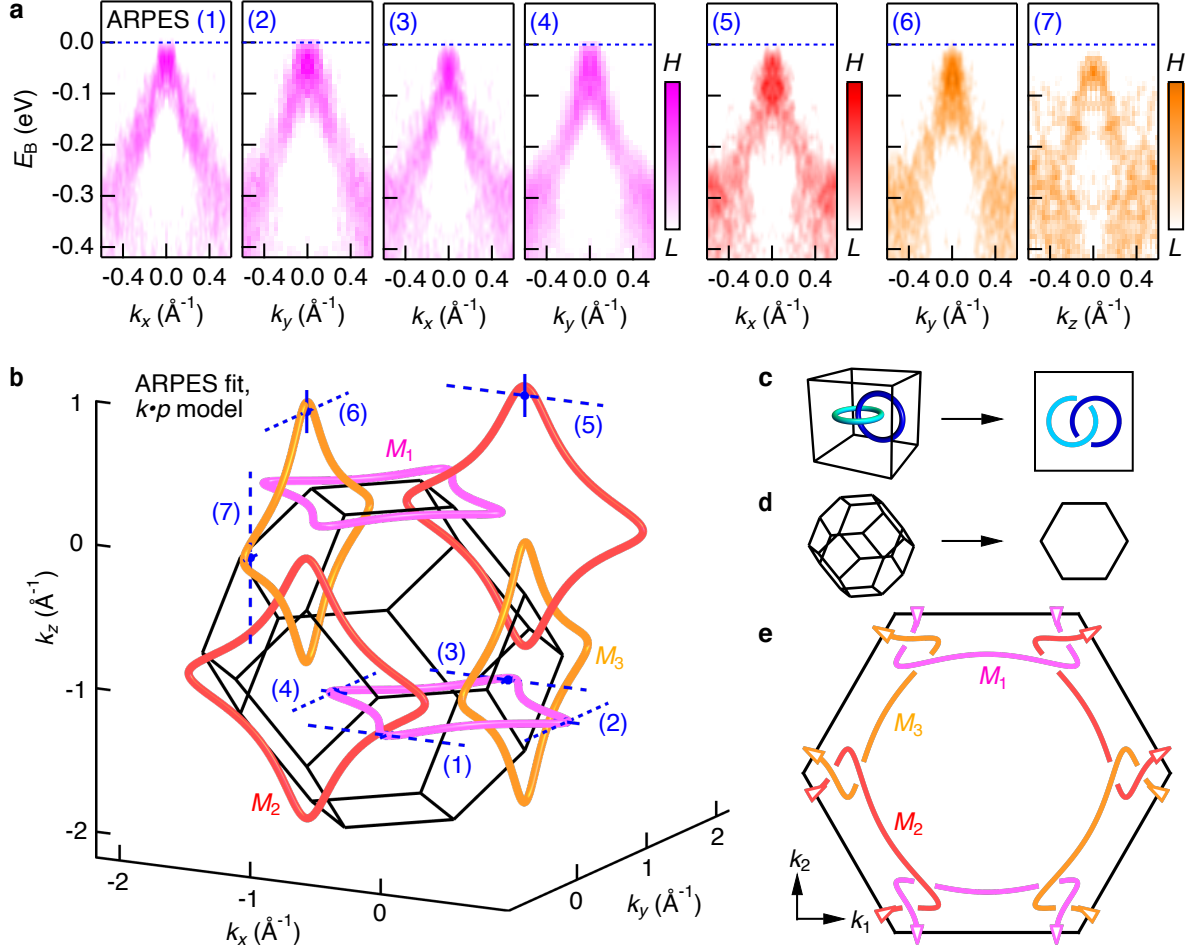


FIG. 4: **Linking number (2, 2, 2) in topological quantum matter.** **a**, Energy-momentum photoemission slices tangential to the M_1 , M_2 and M_3 Weyl loops at their extrema. **b**, Weyl loops from adjacent bulk Brillouin zones, based on the analytical model extracted in Eq. 2 and Fig. 2, exhibiting links. Weyl cone positions (blue dots) extracted from the slices in Fig. 4a (dotted blue lines), consistent with the analytical model (short blue line segments indicate the error). **c**, Link diagrams help visualize a three-dimensional link structure by flattening it to two dimensions while retaining the link information, illustrated for the example of a Hopf link. **d**, In a crystal, it is natural to draw link diagrams in the surface Brillouin zone, such as the (001) surface Brillouin zone (hexagon, Extended Data Fig. 2). **e**, Link diagram for the Co_2MnGa Weyl loop link. There are three distinct Weyl loops and each Weyl loop links each other Weyl loop exactly twice, giving linking number (2, 2, 2). The arrows indicate out-of-plane wrapping: as one follows the loop in the direction of the arrow, the loop wraps out of the page, exiting the Brillouin zone from the front and re-entering from the back, at the same time reconnecting at the opposite edge of the hexagon.

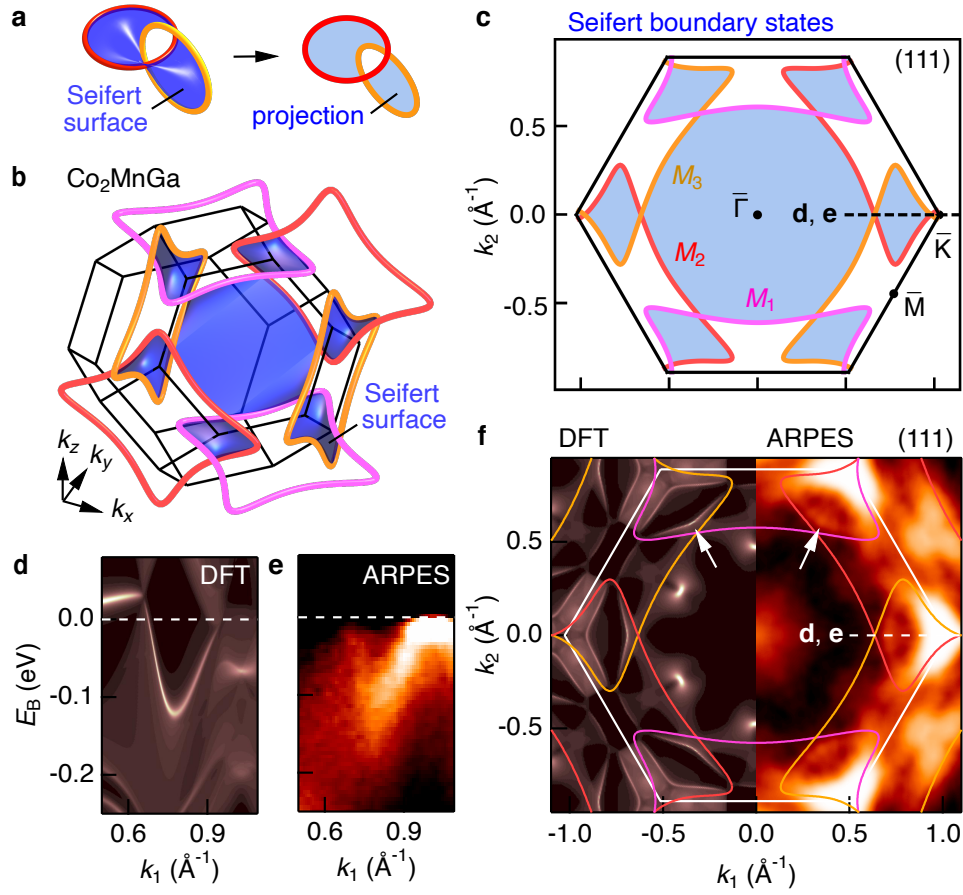
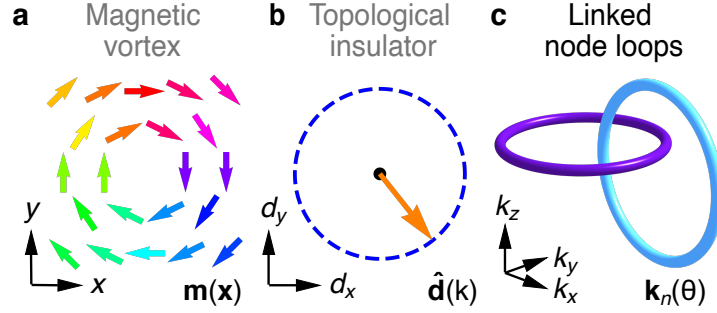
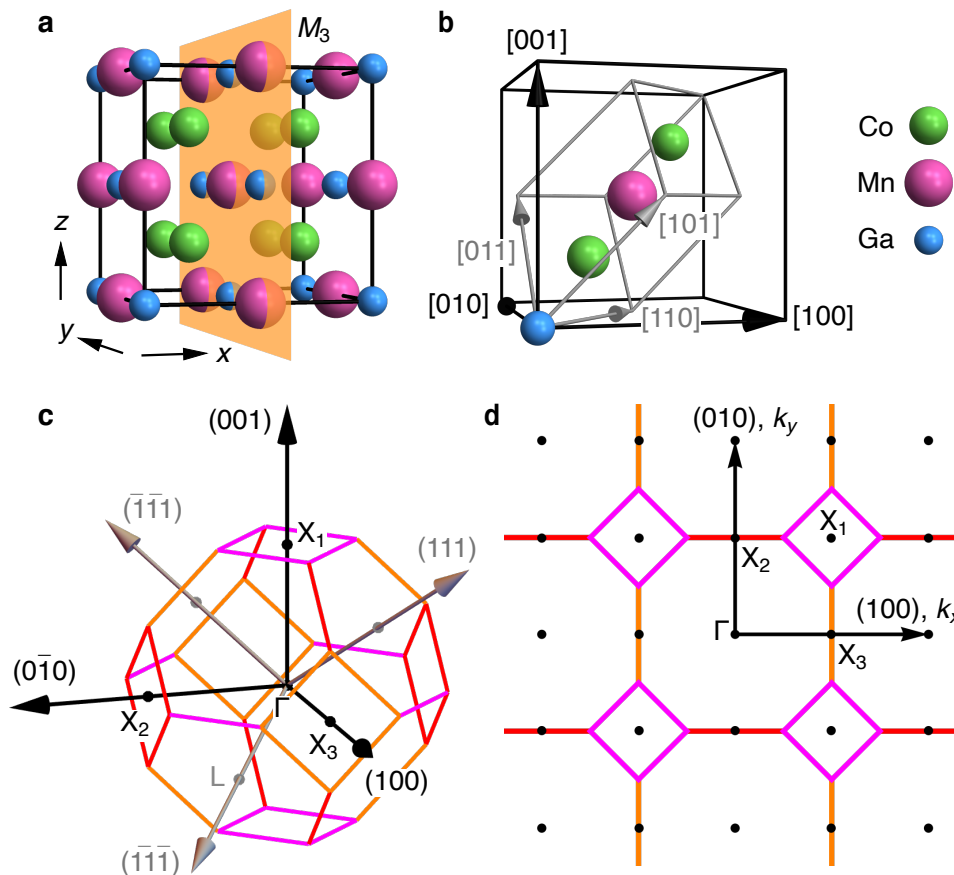


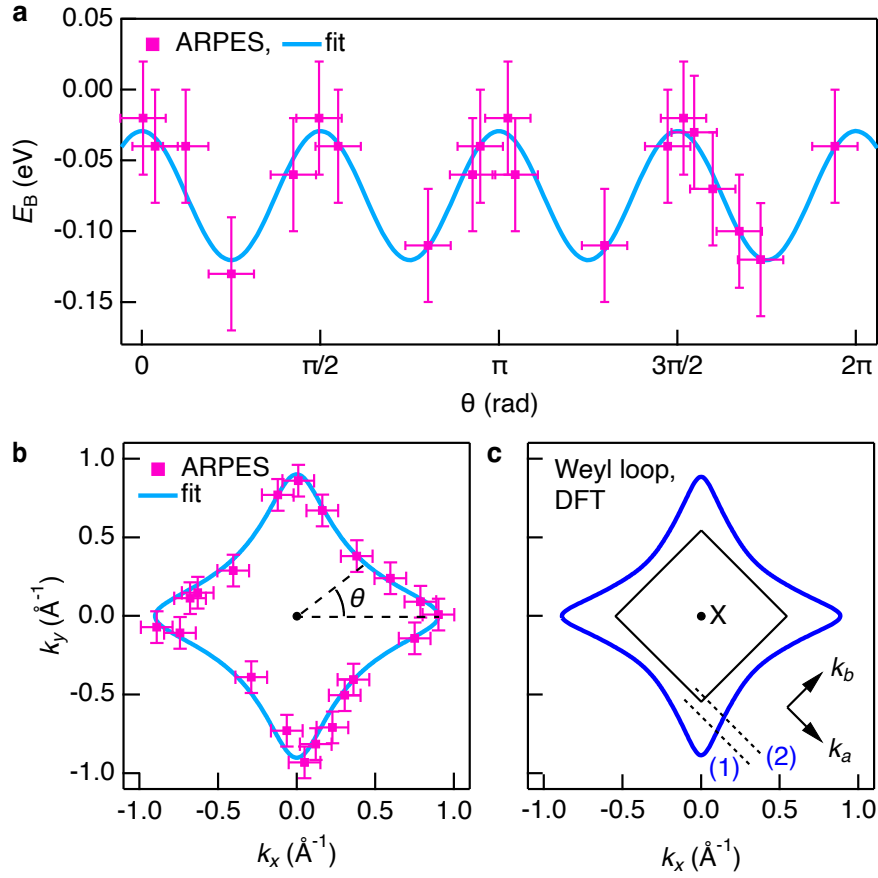
FIG. 5: **Seifert bulk-boundary correspondence.** **a**, A Seifert surface is defined as a three-dimensional surface bounded by a link, shown for the example of a Hopf link. Its two-dimensional projection produces alternating filled and empty regions pinned together at characteristic touching points. **b**, In a condensed matter system, the Seifert surface is taken as a surface bounded by the linked loop nodes in three-dimensional momentum space (k_x, k_y, k_z) , shown for the case of the link observed in Co_2MnGa . **c**, The projection of the Seifert surface into the surface Brillouin zone is associated with topological boundary modes (blue regions) which touch at points in momentum space. Energy axis collapsed for clarity. **d**, *Ab initio* calculation of the surface states through the touching point, exhibiting pairs of boundary modes pinned together at the Weyl loops. **e**, Surface-sensitive vacuum ultraviolet (VUV) ARPES energy-momentum cut through the touching point, exhibiting signatures of the pinned Seifert boundary modes, consistent with *ab initio* calculations. Photon energy $h\nu = 63$ eV. **f**, Fermi surface in *ab initio* calculation (left) and VUV-ARPES (right) exhibiting Seifert boundary modes that stretch across the topological regions, connecting different Weyl loops, consistent with the Seifert projection.



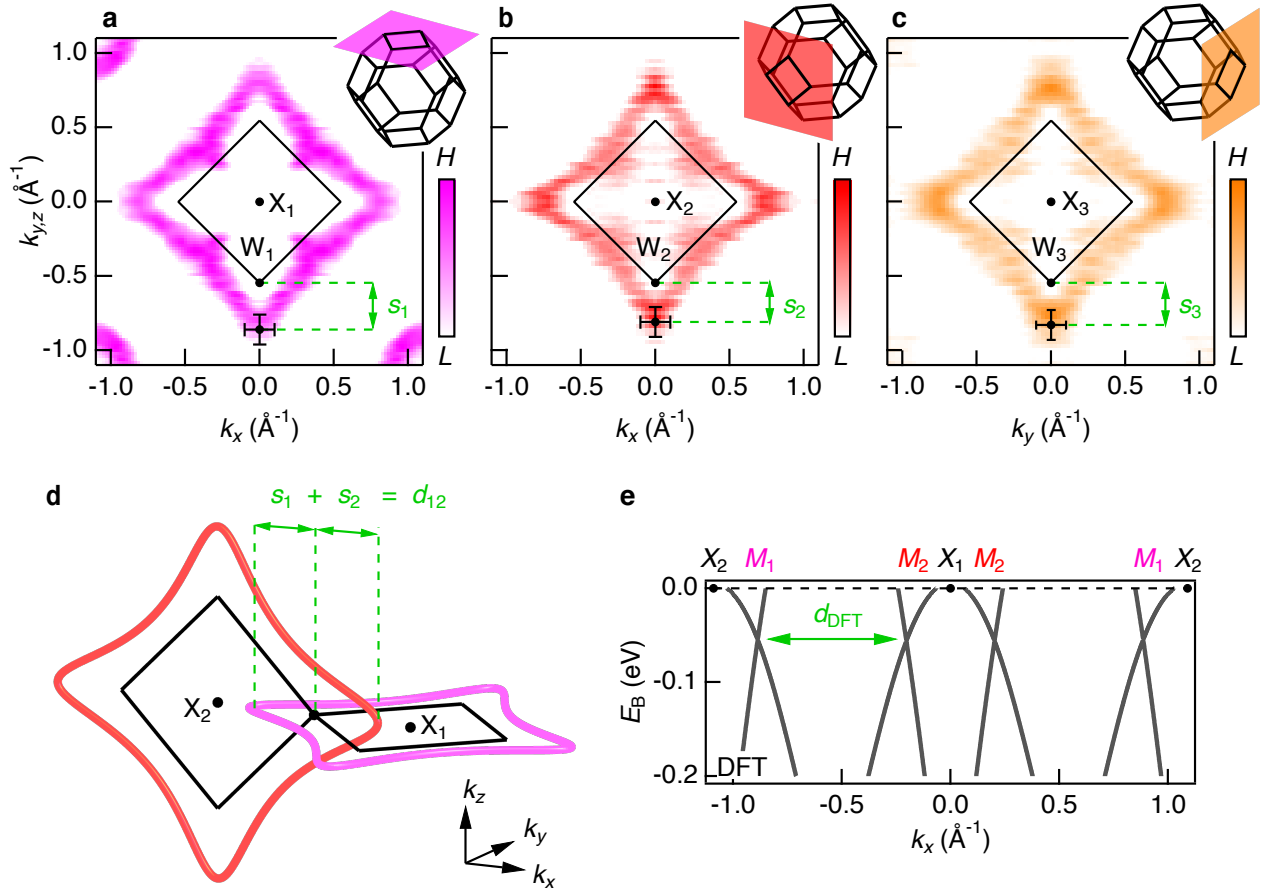
Extended Data Fig. 1: **Topological invariants in physics.** **a**, An example of an order parameter winding in real space: a magnetic vortex. In this case, the order parameter is the local magnetization $\mathbf{m}(\mathbf{x})$, confined to a magnetic easy plane in real space (x, y) . It may happen that $\mathbf{m}(\mathbf{x})$ winds around a point in real space, forming a magnetic vortex characterized by a winding number topological invariant, in this example given by $w = 1$. **b**, An example of a quantum wavefunction winding in momentum space: the one-dimensional topological insulator (Su-Schrieffer-Heeger model). This phase is described by Bloch Hamiltonian $h(k) = \mathbf{d}(k) \cdot \sigma$, where k is the one-dimensional crystal momentum, σ refers to the Pauli matrices and $\mathbf{d}(k)$ is a two-component object confined to the (d_x, d_y) plane. The normalized quantity $\hat{\mathbf{d}}(k) \equiv \mathbf{d}(k)/|\mathbf{d}(k)|$ (orange arrow) moves around the unit circle (dotted blue) as k varies. The topological invariant is related to how many times $\hat{\mathbf{d}}(k)$ winds around the origin as k scans through the one-dimensional Brillouin zone. **c**, Node loops linking in momentum space: a three-dimensional electronic structure may exhibit multiple node loops (cyan and purple), characterized by $\mathbf{k}_n(\theta)$, where n indexes the loops and θ parametrizes the loop trajectory in momentum space. The loops may link one another, encoding a linking number topological invariant. This example shows a Hopf link.



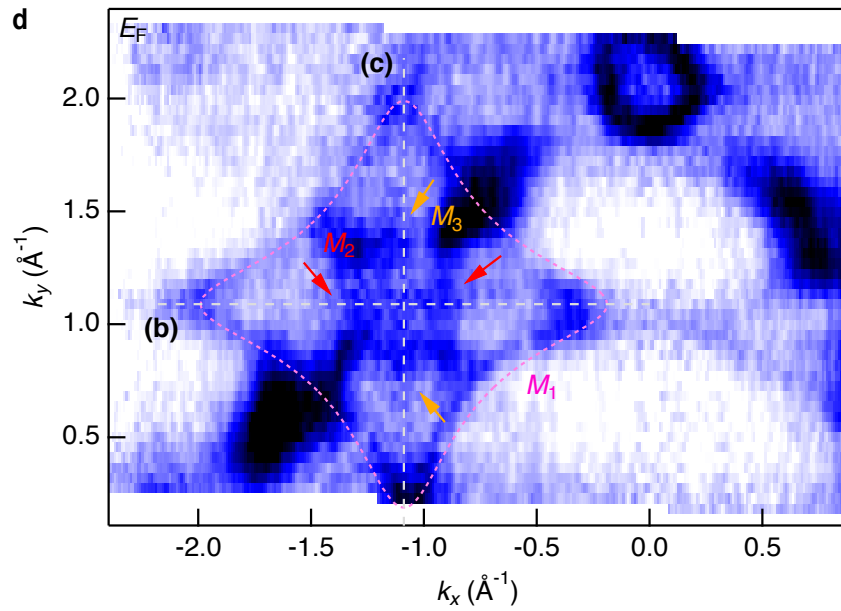
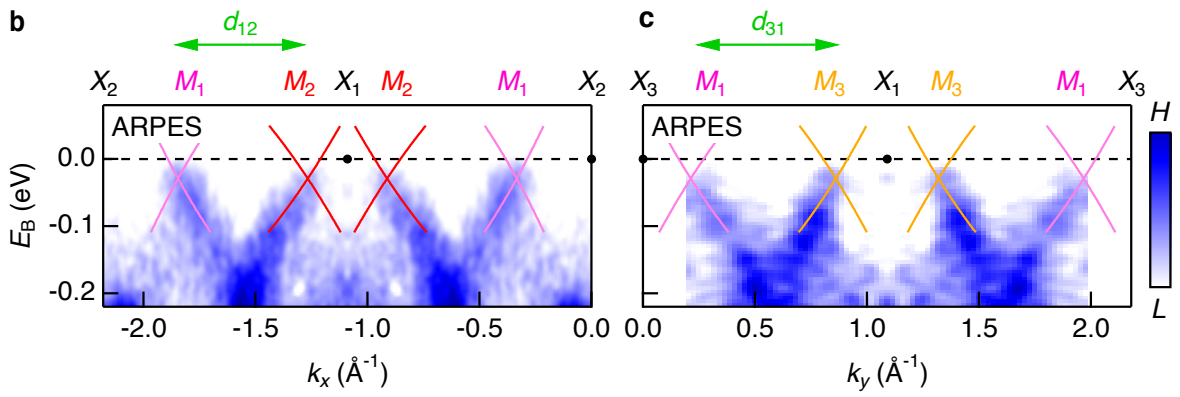
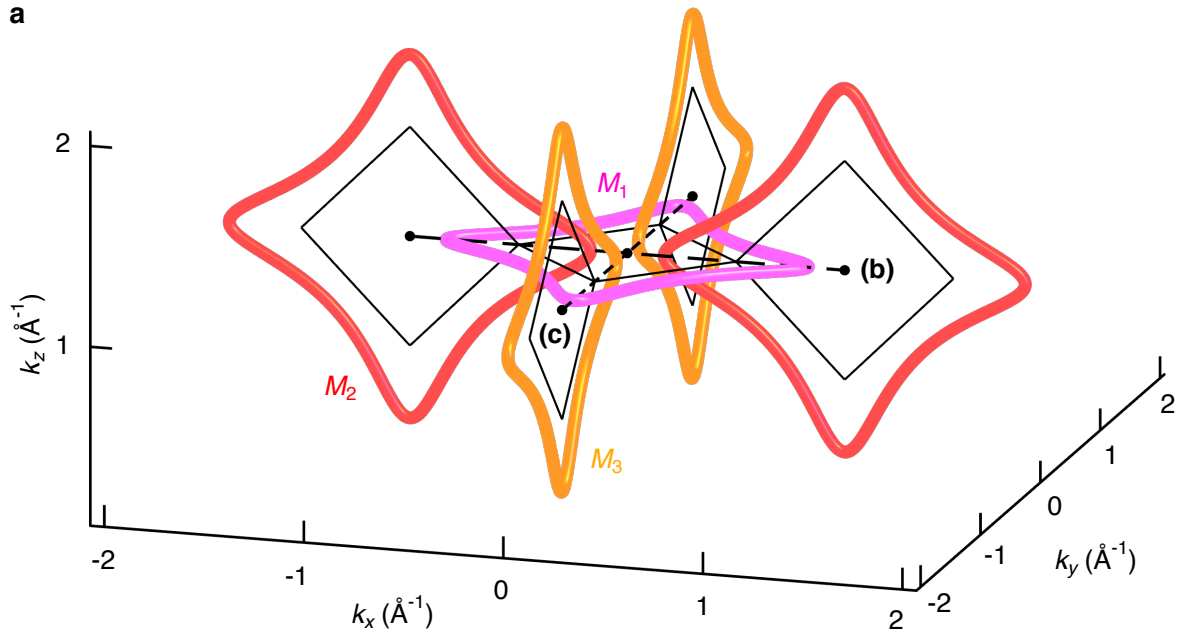
Extended Data Fig. 2: **Crystal structure and Brillouin zone of Co_2MnGa .** **a**, Conventional unit cell with representative crystallographic mirror plane M (orange). **b**, The primitive unit cell (grey) includes one formula unit. **c**, Brillouin zone, with reciprocal lattice basis vectors (grey). In the reciprocal lattice basis, the M_1 plane corresponds to (001) , M_2 corresponds to (010) and M_3 corresponds to (100) . **d**, Slice through Γ in an extended zone scheme.



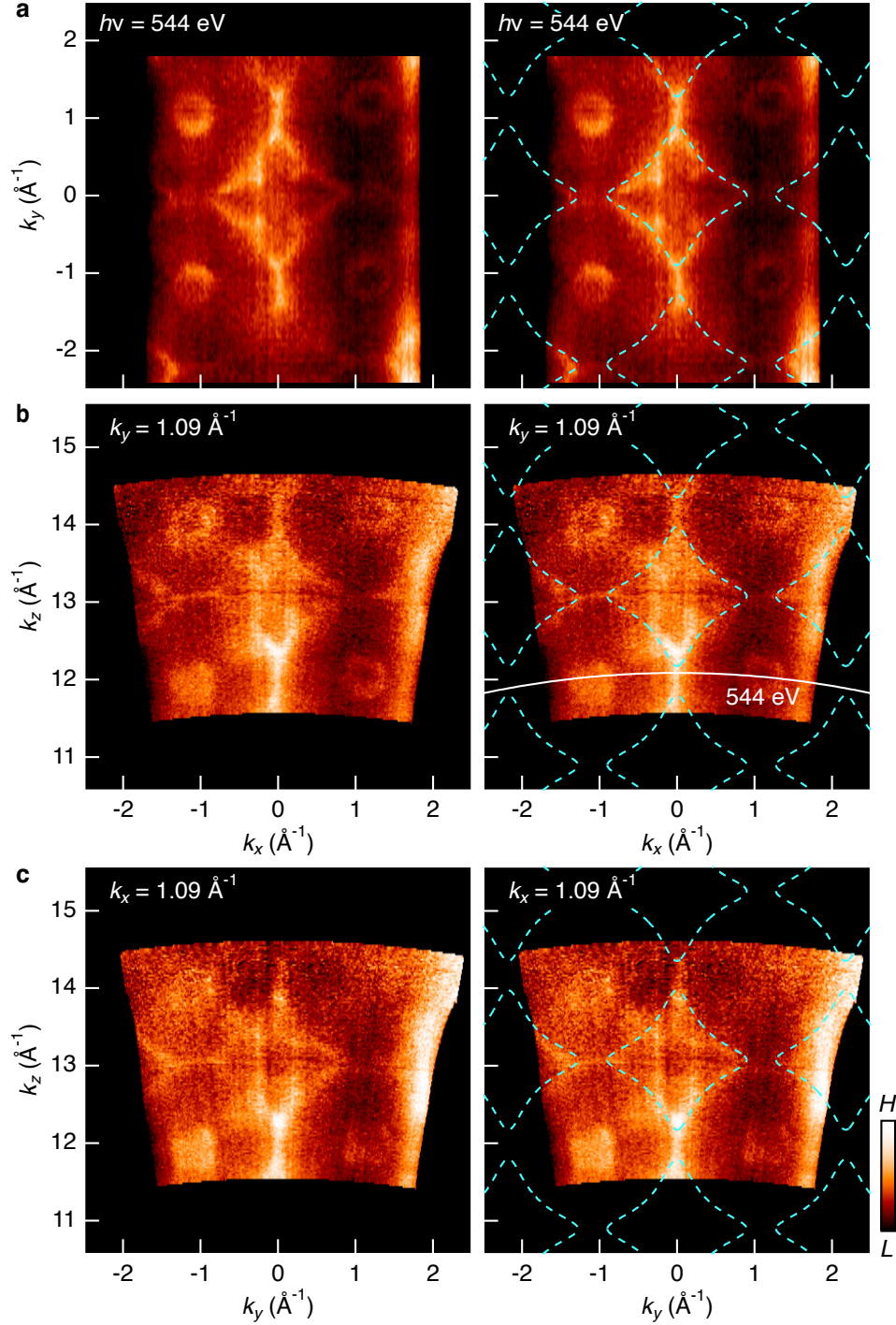
Extended Data Fig. 3: **Energy dispersion of the Weyl loop.** **a**, Crossing point energies E_B and **b**, crossing point momenta (k_x, k_y) systematically extracted from cone dispersions observed in the ARPES spectra (magenta squares), same dataset as Fig. 2c ($h\nu = 544$ eV), with fit of the Weyl loop momentum trajectory and energy dispersion (cyan, see main text). The crossing point energies are parametrized by a polar angle θ defined by $\tan \theta \equiv k_y/k_x$. **c**, Weyl loop trajectory from DFT, with dotted lines indicating the DFT energy-momentum slices shown in Fig. 2b. The binding energy axes in (b) and (c) are collapsed.



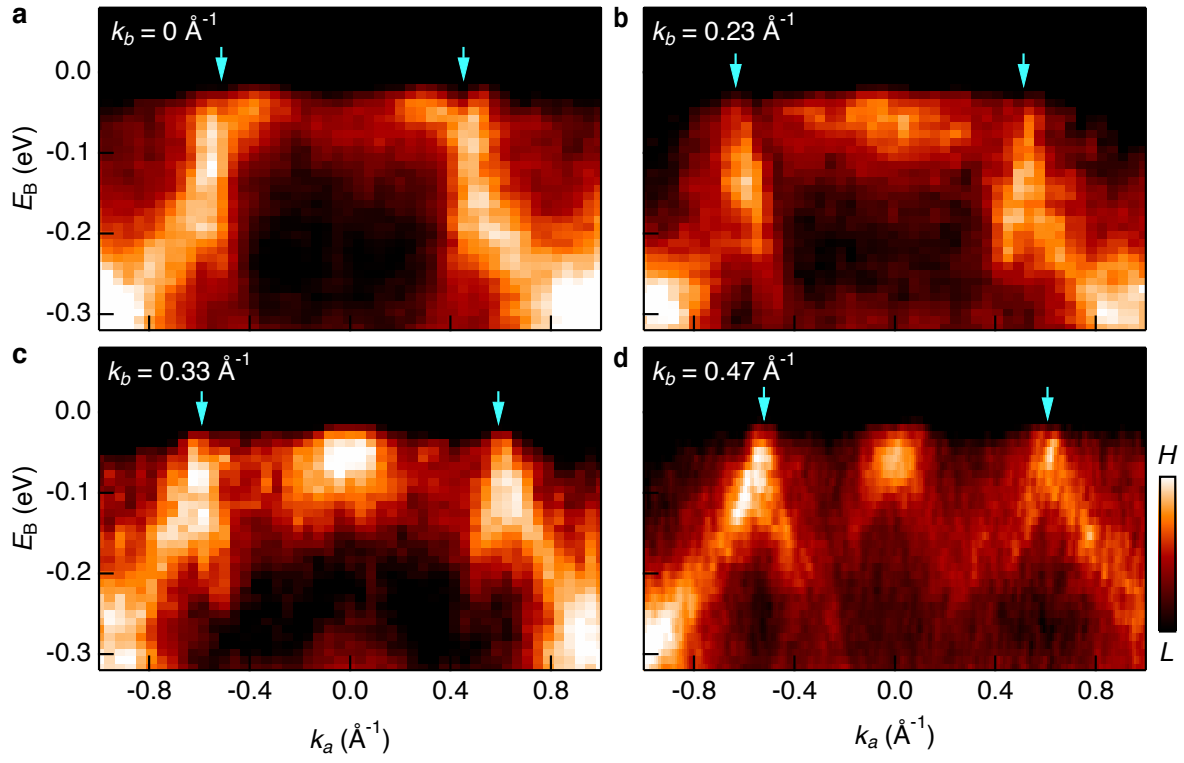
Extended Data Fig. 4: **Link ‘depth’ of the Weyl loops.** **a-c**, Distance between the extrema of the Weyl loops and the bulk Brillouin zone W points for the M_1 , M_2 and M_3 Weyl loops. We estimate $s_1 = 0.32 \pm 0.1 \text{ \AA}^{-1}$, $s_2 = 0.27 \pm 0.1 \text{ \AA}^{-1}$ and $s_3 = 0.29 \pm 0.1 \text{ \AA}^{-1}$. **d**, The link depth captures how far in momentum space one would need to slide the Weyl loops in order to unlink them, providing a measure of the stability of the link. Based on the loop Fermi surfaces (a-c), we estimate $d_{12} = 0.58 \pm 0.14 \text{ \AA}^{-1}$, $d_{23} = 0.55 \pm 0.14 \text{ \AA}^{-1}$ and $d_{31} = 0.60 \pm 0.14 \text{ \AA}^{-1}$. The average gives a typical link depth extracted from ARPES, $d_{\text{avg}} = 0.58 \pm 0.08 \text{ \AA}^{-1}$. **e**, Energy-momentum slice along the high-symmetry path $X_1 - X_2$ from DFT, passing through two linked Weyl loops. We obtain $d_{\text{DFT}} = 0.68 \text{ \AA}^{-1}$.



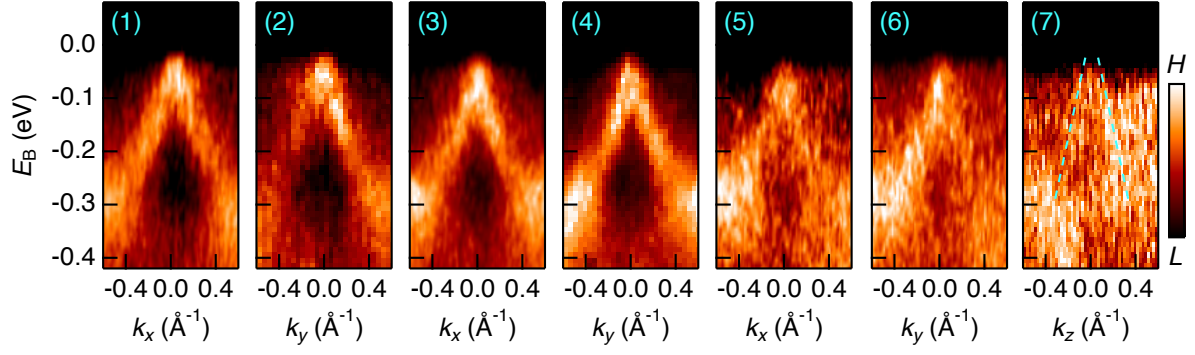
Extended Data Fig. 5: **Supplementary measurement of the link depth.** **a**, M_1 , M_2 and M_3 Weyl loops, with trajectories obtained from the analytical model (see main text), showing that M_1 links M_2 twice and M_3 twice. Energy-momentum photoemission slices along the high-symmetry paths **b**, $X_1 - X_2$ and **c**, $X_3 - X_1$ obtained at photon energy $h\nu = 642$ eV. We observe $d_{12} = 0.56 \pm 0.1 \text{ \AA}^{-1}$ and $d_{31} = 0.61 \pm 0.1 \text{ \AA}^{-1}$, consistent with Extended Data Fig. 4. **d**, Fermi surface acquired at $h\nu = 642$ eV, exhibiting an in-plane Weyl loop contour, M_1 . We further observe spectral weight emanating along k_x and k_y from the center of M_1 , corresponding to the linearly dispersive branches in (**b**, **c**), again suggesting that M_1 is linked by M_2 and M_3 .



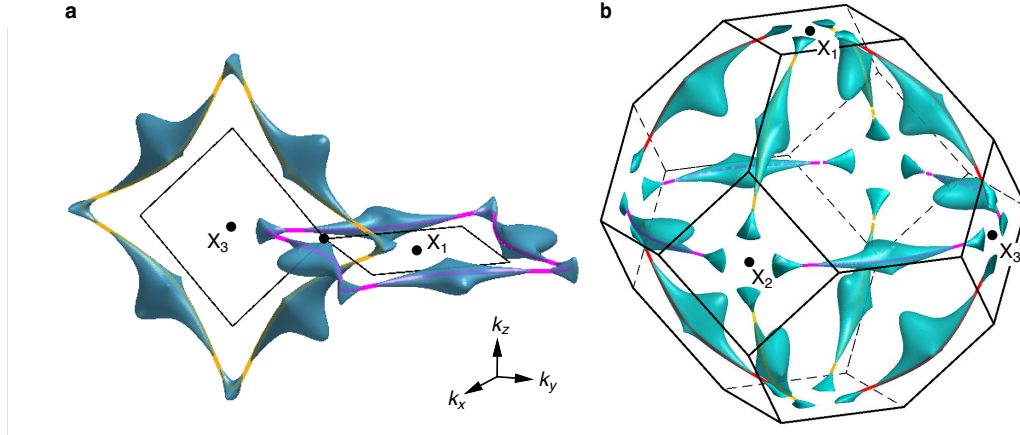
Extended Data Fig. 6: **Unsymmetrized Fermi surfaces.** **a-c**, Left: photoemission spectra displayed in Fig. 1d-f, without symmetrization. Right: the same spectra, with the experimentally-determined Weyl loop trajectory overlaid across multiple Brillouin zones. The irrelevant Γ pocket is consistently observed in all unsymmetrized spectra. Signatures of Weyl loops are observed around all X points.



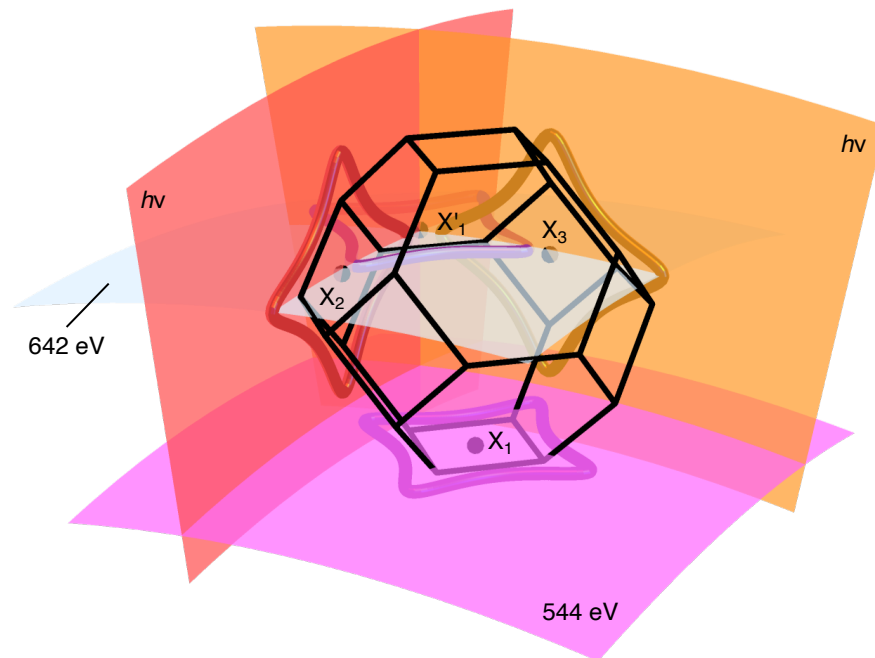
Extended Data Fig. 7: **Energy-momentum cuts through the Weyl loop.** Photoemission spectra used to extract Fig. 2c.



Extended Data Fig. 8: **Unsymmetrized energy-momentum cuts.** Photoemission spectra displayed in Fig. 4a, without symmetrization.



Extended Data Fig. 9: **Linked Weyl loop Fermi surface.** Constant-energy slice of the pockets (navy) making up two linked Weyl loops obtained by *ab initio* calculation, at binding energy $E_B = -10$ meV, below the experimental Fermi level. The Fermi surface pockets touch at a set of discrete points, where the Weyl loop disperses through this particular E_B . For reference, the full Weyl loop trajectories are indicated, collapsed in energy (orange around X_3 , magenta around X_1). We observe that the Weyl loop Fermi surface pockets form a linked structure.



Extended Data Fig. 10: **Measured Fermi surfaces in an extended zone scheme.** The Brillouin zone corresponds to $\Gamma_{(066)}$ in the primitive reciprocal basis.